

communications materials

ARTICLE



<https://doi.org/10.1038/s43246-021-00149-8>

OPEN

Cryogenic toughness in a low-cost austenitic steel

Yuhui Wang¹, Yubin Zhang², Andrew Godfrey³✉, Jianmei Kang¹, Yan Peng¹, Tiansheng Wang^{1,4}, Niels Hansen⁵ & Xiaoxu Huang^{2,6}✉

At low temperatures most metals show reduced ductility and impact toughness. Here, we report a compositionally lean, fine-grained Fe-30Mn-0.11C austenitic steel that breaks this rule, exhibiting an increase in strength, elongation and Charpy impact toughness with decreasing temperature. A Charpy impact energy of 453 J is achieved at liquid nitrogen temperatures, which is about four to five times that of conventional cryogenic austenitic steels. The high toughness is attributed to manganese and carbon austenite stabilizing elements, coupled with a reduction in grain size to the near-micrometer scale. Under these conditions dislocation slip and deformation twinning are the main deformation mechanisms, while embrittlement by α' - and ϵ -martensite transformations are inhibited. This reduces local stress and strain concentration, thereby retarding crack nucleation and prolonging work-hardening. The alloy is low-cost and can be processed by conventional production processes, making it suitable for low-temperature applications in industry.

¹National Engineering Research Center for Equipment and Technology of Cold Rolled Strip, Yanshan University, Qinhuangdao, China. ²Department of Mechanical Engineering, Technical University of Denmark, Lyngby, Denmark. ³Laboratory of Advanced Materials (MoE), School of Material Science and Engineering, Tsinghua University, Beijing, China. ⁴State Key Laboratory of Metastable Materials Science and Technology, Yanshan University, Qinhuangdao, China. ⁵Risø Campus, Technical University of Denmark, Roskilde, Denmark. ⁶International Joint Laboratory for Light Alloys (MOE), College of Materials Science and Engineering, Chongqing University, Chongqing, China. ✉email: awgodfrey@mail.tsinghua.edu.cn; xiaoxuhuang@cqu.edu.cn

Low-temperature metals and alloys are widely used in industry, covering a broad range of areas including liquefied natural gas (LNG) tanks, ice-breakers, cryogenic superconductivity, and outer space exploration¹. For such applications, high cryogenic impact toughness is desired to prevent catastrophic failure during impact loading². A general challenge here is that impact toughness in metals and alloys almost invariably decreases with decreasing temperature. As such, the conventional metals and alloys that have been developed for low-temperature applications, including steels^{3,4}, Ti⁵, and Al⁶, have relatively low impact toughness at cryogenic temperatures, limiting their application at such service temperatures. Solutions to this problem have been explored, though all with significant drawbacks in terms of cost. For example, a mature class of alloys based on 9% Ni has been developed over the last 60 years and is used widely for the construction of LNG tankers¹. The fracture toughness of these alloys is still, however, limited only to moderate values (<100 J). Moreover, to achieve the required properties in these alloys, ultrapure smelting technology and complex heat treatments are required^{7,8}, resulting in high production costs. It remains therefore a dream in material science to develop cheap, industrially practical alloys with toughness that remains unchanged or even increases, at low temperatures.

An inverse temperature dependence of toughness has, in fact, been reported recently for a ferritic steel with an ultrafine-grain structure³, where the enhanced toughness was attributed to fine scale delamination resulting from crack branching on aligned crystallographic cleavage planes. The inverse temperature dependence of toughness only holds, however, down to a moderately low temperature of -50°C , with a corresponding maximum impact energy of about 300 J. At lower temperatures the toughness decreases dramatically in the usual manner. More recently, an increase in impact toughness with decreasing temperature has also been reported for some high- and medium-entropy alloys (HEAs/MEAs), e.g., CrMnFeCoNi, where an exceptionally high cryogenic impact toughness of ~400 J has been achieved^{9,10}. Despite this high cryogenic impact toughness, such alloys are likely to have only limited industrial application, as a result both of the high cost associated with the required amounts of expensive alloying elements (especially Co), and due to the complexity of large-scale production of components using HEAs and MEAs¹¹. The sustainability of such alloys is also a challenge, due to difficulties in recyclability associated with the large alloying fractions used in HEAs and MEAs.

Two lessons that can be learned from the studies on HEAs are, however, important. These are: (i) that an ultrahigh impact energy can be achieved by enabling a transition with decreasing temperature from planar-slip dislocation activity at room temperature (RT) to deformation by mechanical nanotwinning at lower temperatures, and (ii) that to achieve an inverted toughness-temperature relationship, both strength and ductility should simultaneously increase with decreasing test temperature^{8,12}. The first criterion can be fulfilled in some cost-effective high-Mn austenitic steels^{13,14}. However, in these alloys HCP ϵ - and BCC α' -martensitic transformation can take place during plastic deformation at low temperatures, or even in some cases during cooling¹⁵, which leads to embrittlement and hence premature fracture and low fracture toughness^{16,17}. The martensitic transformation can be suppressed to a certain extent by increasing the Mn, Al, Si, or C content^{18–23} or via grain refinement^{24–27}. By use of these approaches, the highest cryogenic toughness value for a high-Mn steel presently achievable is about 220 J^{15,16,22}. Regarding the second criterion, a survey of the literature reveals one Fe30Mn steel²⁸ and some FeMnAl alloys²⁹ that exhibit an increase in both strength and ductility with decreasing temperature, though whether an inverse temperature dependence of toughness holds for these steels is not reported.

Inspired by these studies, here we report data for a fine-grained (mean grain size of $5.6\ \mu\text{m}$) Fe-30Mn-0.11C austenitic steel. The choice of composition is based on previously reported promising results for a Fe30Mn steel²⁸, with the addition of a small amount of C as an additional austenite stabilizing element. In combination with appropriate grain refinement the resulting steel is resistant to the formation of ϵ martensite^{20,24–27} during low-temperature deformation^{20,24–27}. The results show that this steel can satisfy both of the criteria listed above, and also exhibit an unusual increase in toughness with decrease of temperature to the cryogenic regime, leading to an ultrahigh Charpy impact energy exceeding 450 J at liquid nitrogen temperature (LNT, 77 K). In addition, the steel consists of only two elements of the Cantor HEA, together with a small amount of carbon, and is produced by a process involving only conventional cold rolling and annealing. The simple alloy composition, low cost, and conventional processing route are expected to enable a broad range of cryogenic applications for this alloy.

Results

Tensile behavior at RT and LNT. Figure 1a shows the microstructure and engineering tensile stress-strain curves at RT and LNT for the Fe-30Mn-0.11C alloy in both a fine-grained (mean grain size of $5.6\ \mu\text{m}$; Fig. 1c, d) and coarse-grained (mean grain sizes of $47.0\ \mu\text{m}$; Fig. 1e, f) condition. The stress-strain curves for both samples display continuous (nonserrated) flow at both RT and LNT. At both temperatures, the decrease in grain size from 47.0 to $5.6\ \mu\text{m}$ leads to increases in the yield strength (0.2% offset) and ultimate tensile strength (UTS) of about 25% and 7–10%, respectively, with a corresponding small reduction in total elongation (see Table 1). It is notable, however, that as the temperature is decreased from RT to LNT, both the yield strength and UTS, as well as the ductility, show a remarkable simultaneous increase, of about 55% for the yield strength and UTS and 30–40% for the ductility. The work-hardening rates, calculated from the true stress–true strain curves, are shown in Fig. 1b. It can be seen that at both temperatures, extensive work-hardening ability of the steel is achieved without premature failure (i.e., the flow curves are indicative of ductile failure following the *Considère* plastic instability criterion), in contrast to observations in twinning-induced plasticity (TWIP) steels where strain localization leads to premature failure^{30,31}.

To understand these mechanical properties, the microstructures of the two samples in uniformly deformed regions have been examined in the scanning electron microscope (SEM) and the transmission electron microscope (TEM). These observations reveal that in the as-processed condition, the steel has a fully austenitic recrystallized structure and contains annealing twins, similar to other austenitic steels (Fig. 1c–f)^{15,16,22,23,28,30,32}. In the fine-grain size condition, the major deformation mode during tensile testing at RT is found to be dislocation slip. SEM observations using electron backscatter diffraction (EBSD) show that no α' martensite or ϵ martensite is formed either along grain boundaries or in the grain interior regions (Fig. 2a, b), and TEM observations confirm the presence of a dislocation-based deformation microstructure (Fig. 2c) without evidence of deformation twinning. In fine-grain size samples tensile tested at LNT, TEM observations show the presence of extensive deformation twinning, again though without any evidence of martensitic transformation (see Fig. 2d–f). A similar deformation response is seen for the coarse-grained sample (see Fig. 2g–l). The results reveal that for both grain sizes, deformation-induced nanotwin formation is a dominant deformation mechanism at LNT, while dislocation motion, associated with glide of $1/2<110>$ dislocations on $\{111\}$ planes, is the main deformation mechanism at RT. It is worth

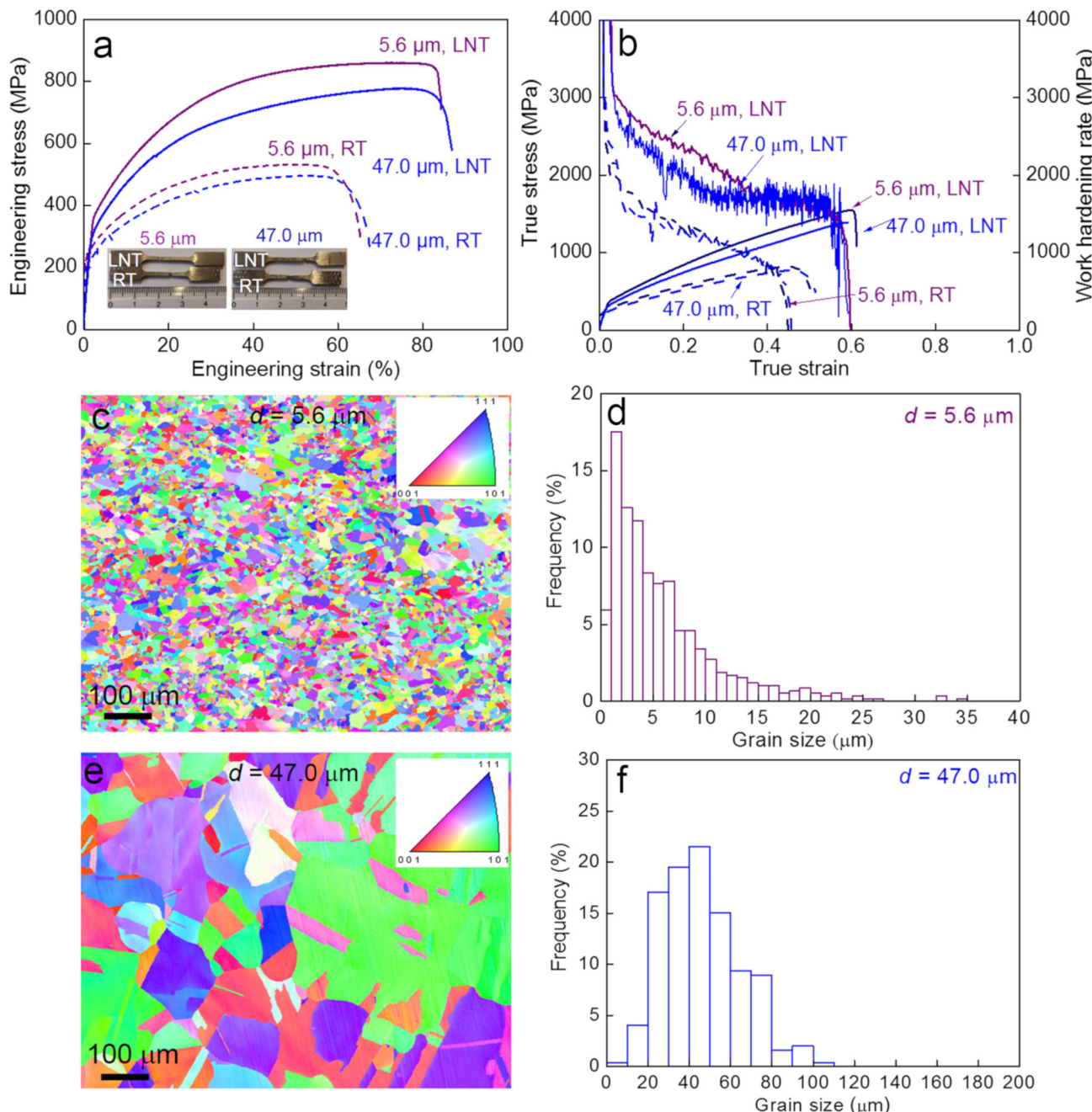


Fig. 1 Microstructures and tensile properties at RT and LNT for fine- and coarse-grained samples. **a**, Engineering stress–strain curves for fine- and coarse-grained samples under uniaxial tension testing at RT and LNT. Yield strength, ultimate tensile strength, and ductility (strain to failure) of the fine- and coarse-grained samples simultaneously increase with decreasing deformation temperature from RT to LNT. **b**, Work-hardening rate and true stress as a function of true strain, showing extensive work hardening before ductile failure following the Considère criterion. **c**, Inverse pole figure (IPF) map of fully recrystallized microstructure in the fine-grained sample. **d**, Grain size distribution in the fine-grained sample. **e**, Inverse pole figure (IPF) map of fully recrystallized microstructure in the coarse-grained sample. **f**, Grain size distribution in the coarse-grained sample.

noting that with decreasing grain size, the fraction of grains that undergo mechanical twinning at LNT decreases, and the dislocation density inside the nanotwins increases.

Super toughening mechanism. Both the microstructural characterization and the mechanical results suggest that the present steel fulfills the two criteria proposed above for an inverse temperature–toughness dependence. Charpy impact tests were therefore conducted to verify this hypotheses. During testing none of the samples broke into two separate pieces,

demonstrating their excellent toughness (see Supplementary Fig. 1). Indeed, we found that for the fine-grained samples, the impact toughness increased by 36% as the test temperature was lowered from RT to LNT. Moreover, an extraordinary low-temperature toughness of more than 450 J at LNT was obtained for the fine-grained sample (see Table 2), representing to the authors' knowledge a new record at present for all reported metals and alloys^{9,15,16,22,33–38}. Interestingly, the impact toughness for the coarse-grained sample follows the normally expected toughness–temperature dependence, with a toughness decrease of ~38% as the temperature is lowered from RT to LNT.

Table 1 Tensile properties at RT and LNT for Fe30Mn-0.11C steel samples with fine (5.6 μm) and coarse (47.0 μm) mean grain size.

Sample	RT			LNT		
	Yield strength (MPa)	Ultimate tensile strength (MPa)	Uniform elongation (%)	Total elongation (%)	Yield strength (MPa)	Ultimate tensile strength (MPa)
Mean grain size (μm)	180 \pm 2.0	495 \pm 11.0	53 \pm 3.8	66 \pm 1.7	280 \pm 5.0	777 \pm 31
47.0 \pm 4.0	230 \pm 15	531 \pm 5.0	50 \pm 2.7	65 \pm 2.9	360 \pm 3.0	860 \pm 15

In order to explain the impact toughness results, we also characterized the microstructure in regions close to the fracture surface of impact-tested samples (see Fig. 3 and Supplementary Fig. 2). For the fine-grained samples, deformation-induced twinning is prevalent both in samples tested at RT and LNT, though is more pronounced at the lower temperature. Significantly, neither α' nor ϵ martensite are detected in the fine-grained sample after Charpy impact testing both at RT and at LNT (see Fig. 3a–e), in agreement with the results obtained from tensile testing. Example fractographs of the fine-grained samples after Charpy impact testing at RT and LNT are shown in Fig. 3j–l. At both temperatures, the fracture surfaces are mostly composed of dimples of submicrometer or greater depth. Beneath the fracture surfaces, only a small amount of cavities is seen (see Supplementary Fig. 3).

For the coarse-grained samples, extensive deformation twinning is seen after Charpy impact testing at both RT and LNT. Notably, some ϵ -martensite formation is found for samples tested at LNT (see Fig. 3f–i). The difference in deformation behavior compared to tensile testing is likely to originate in the much higher strain rate during Charpy impact testing. The formation of ϵ martensite and its interaction with other ϵ -martensite and grain boundaries contributes to the reduced impact toughness of the coarse grain material at LNT^{18–20,31}.

To further understand the high impact toughness values, the three-dimensional (3D) fracture surface morphology after Charpy impact testing at LNT was characterized using 3D microcomputed tomography (micro-CT). For the fine-grained sample, a large neck is seen together with secondary cracking (Fig. 4a), whereas only a single deep crack is seen in the coarse-grained sample (Fig. 4b). The plastic deformation around the crack is more pronounced for the fine-grained sample, extending to regions further beyond the notch, while for the coarse-grained sample the plastic deformation is concentrated mainly in the region close to the two notch surfaces (see Table 3). Stress concentrations due to the formation of the ϵ martensite (see Fig. 3) are likely to be the reason for the less pronounced plastic deformation and for the development of just a single deep crack in this coarse-grained sample, both of which contribute to the reduced Charpy toughness.

Comparison with various cryogenic metals. Several alloys, including 304L and 316 austenitic stainless steel and 9% Ni steel, have already been successfully used in cryogenic applications^{1,33,36}. Recently, great efforts have been made to develop high-manganese TWIP austenitic steels for cryogenic applications. Figure 5 compares the Fe-30Mn-0.11C steel of the present work with a number of alloys that have been used or proposed for cryogenic applications. As seen in Fig. 5a the Fe-30Mn-0.11C alloy achieves a very high impact toughness at a Mn concentration lower than that (34%) required to give maximum toughness in the Fe-Mn binary system. In Fig. 5b it is seen that for the same level of yield strength, the Charpy impact energy of the fine-grained Fe-30Mn-0.11C steel is significantly higher (4–5 times) compared to the 304(L) and 316(L) steels, and noticeably higher compared to the HEAs/MEAs. Recently, a Charpy impact energy of 398 J at LNT was obtained in CrCoNi MEA, representing at that time the highest reported value for all known alloys³⁷. The present fine-grained Fe-30Mn-0.11C alloy shows, however, a LNT impact toughness exceeding this by more than 50 J.

Although 9% Ni steel is well established as a cryogenic alloy, it is expected that the HEAs/MEAs may replace both the 9% Ni alloy and stainless steels, for some extreme-environmental cryogenic applications^{37–39}. A challenge here, however, concerns the high cost of Ni and Co for both the 9% Ni steels and

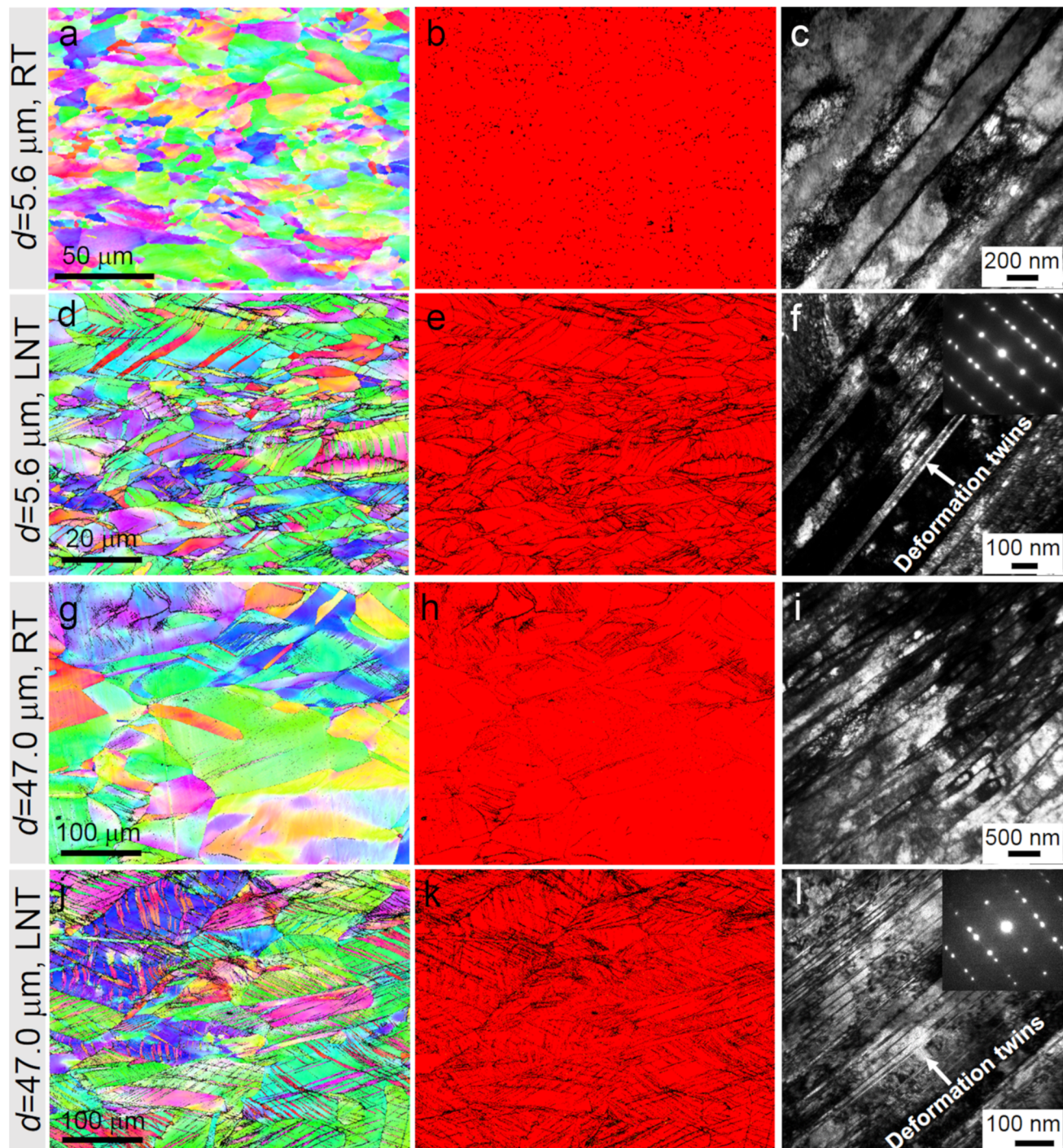


Fig. 2 Deformation mechanisms of fine- and coarse-grained samples after tensile tested at RT and LNT. **a** EBSD inverse pole figure (IPF) map and **b** the corresponding phase map shows the structure to be single-phase austenite with no martensite detected. **c** TEM image shows dislocation arrangements in the fine-grained sample after tensile testing at RT. **d** EBSD IPF map and **e** the corresponding phase map with no martensite detected. **f** TEM image shows numerous deformation twins in the fine-grained sample after tensile testing at LNT. **g** EBSD IPF map and **h** the corresponding phase map with no martensite detected. **i** TEM image shows dislocation arrangements in the coarse-grained sample after tensile testing at RT. **j** EBSD IPF map and **k** the corresponding phase map with no martensite detected. **l** TEM image shows dislocations of the coarse-grained sample after tensile tested at LNT.

CoCrFeNi HEAs/CrCoNi MEAs, as discussed further in the outlook presented at the end of this work.

Discussion

Similar to the Fe30Mn alloy comprising austenite grains of 20–50 μm ²⁸, both fine- and coarse-grained Fe-30Mn-0.11C alloys

exhibit a remarkable simultaneous increase in both the yield strength and UTS, as well as the ductility, as the testing temperature decreases from RT to LNT. However, even for the coarse-grained Fe-30Mn-0.11C alloy the impact energy is about twice that for a Fe30Mn steel (see Fig. 5a), and is still somewhat higher than the maximum value achieved in the Fe-Mn binary system for a Fe-36Mn steel¹⁶. Although the grain sizes of these

two Fe–Mn binary alloys were not reported, it is expected that the grain sizes in these two alloys are similar to that of the coarse-grained sample, as the processing conditions for these alloys are similar¹⁵. The addition of 0.11% C to the Fe-30Mn steel provides additional stabilization of the austenite phase, leading to a reduction in the extent of α' - and ϵ -martensitic transformation

during deformation, while at the same time providing additional solution hardening^{21,28,40}. Moreover, the results show also that compared to the Fe-36Mn steel^{15,16}, addition of 0.11% of C is more effective than the 6% Mn in achieving a high LNT impact toughness, presumably due in part to the extensive interaction of C with dislocations, which contributes, in addition to the mechanical twinning, to a mechanism for sustained work hardening⁴⁰. The combination of both the increased strength and the work-hardening ability is expected to contribute to the high impact energy.

Remarkably, the low-temperature impact energy for the fine-grained Fe-30Mn-0.11C steel is nearly twice that of the coarse-grained steel of the same composition. Evidently, the grain size plays a dominant role in enabling the observed inverted temperature-toughness dependence and the high cryogenic impact toughness. For several carbon steels with medium-high Mn content (15–22 wt.%) including TWIP steels, it has been reported that ϵ -martensite transformation was suppressed by a reduction of grain size^{26,27,31}. However, in these steels embrittlement by ϵ martensite is not completely eliminated, due to the comparatively low Mn content^{1,26,31}. As a result, the ductility of

Table 2 Charpy impact energy (C_{ev}) at RT and LNT for the Fe-30Mn-0.11C steel for fine (5.6 μm) and coarse (47.0 μm) mean grain size.

Mean grain size (μm)	LNT		RT	
	C_{ev} (J)	Average (J)	C_{ev} (J)	Average (J)
47.0 (coarse)	265	269 \pm 16	378	372 \pm 5
	290		372	
	251		365	
5.6 (fine)	458	453 \pm 4	335	334 \pm 4
	448		329	
	452		340	

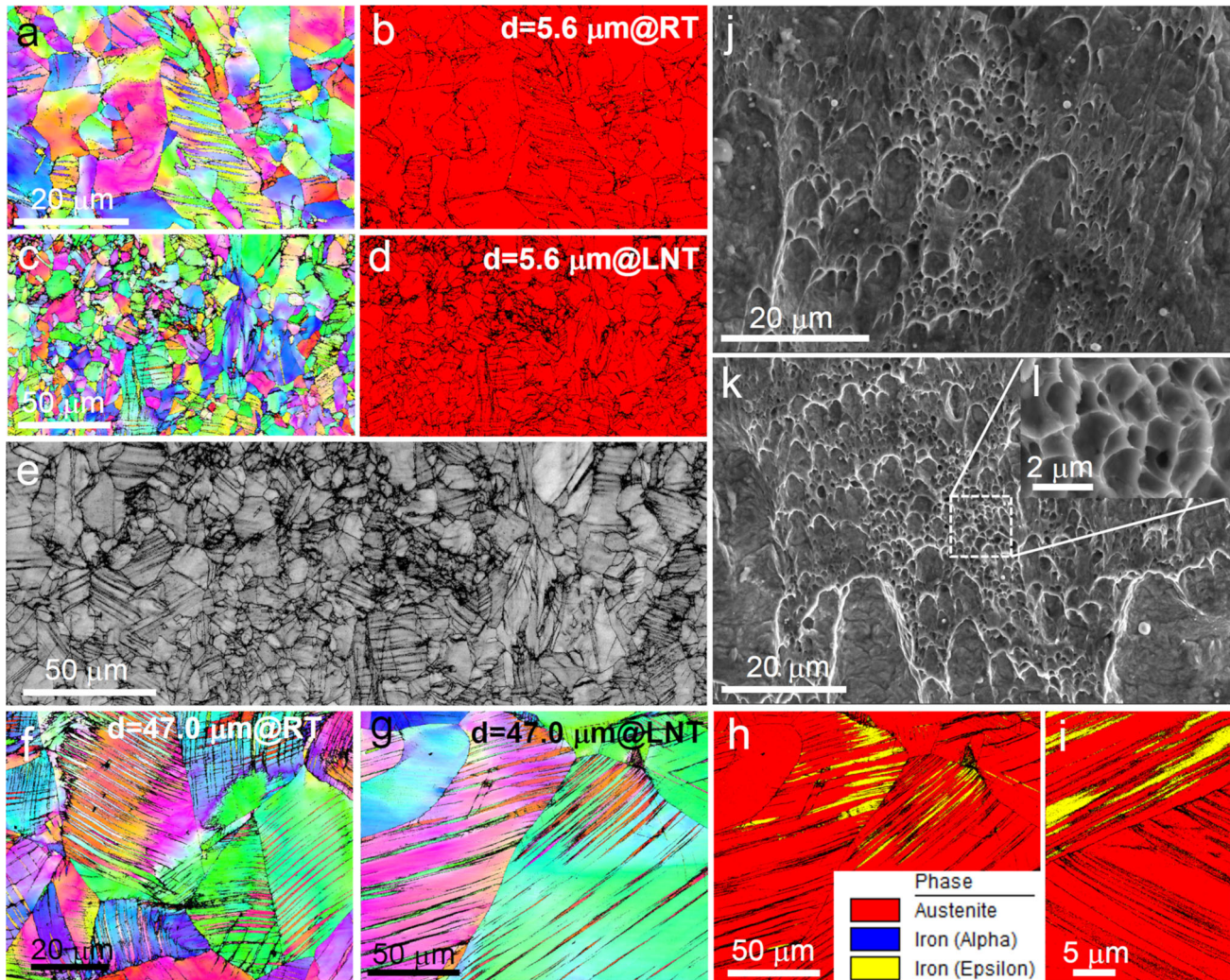


Fig. 3 Microstructure of samples at regions about 1000 μm from the fracture surface after impact testing at RT and LNT. **a** EBSD IPF map of fine-grained sample after Charpy impact testing at RT and **b** corresponding EBSD phase map. **c** EBSD IPF map of fine-grained sample after Charpy impact testing at LNT and **d** corresponding phase map and **e** image quality (IQ) map. **f** EBSD IPF map of coarse-grained sample after Charpy impact testing at RT. **g** EBSD IPF map of coarse-grained sample after Charpy impact testing at LNT and **h** corresponding phase map and **i** enlargement of ϵ -martensite region. **j** SEM fractograph of the fine-grained sample after Charpy impact testing at RT. **k** SEM fractograph of the fine-grained sample after Charpy impact testing at LNT and **l** a high magnification view of **k** showing the presence of small fracture dimples.

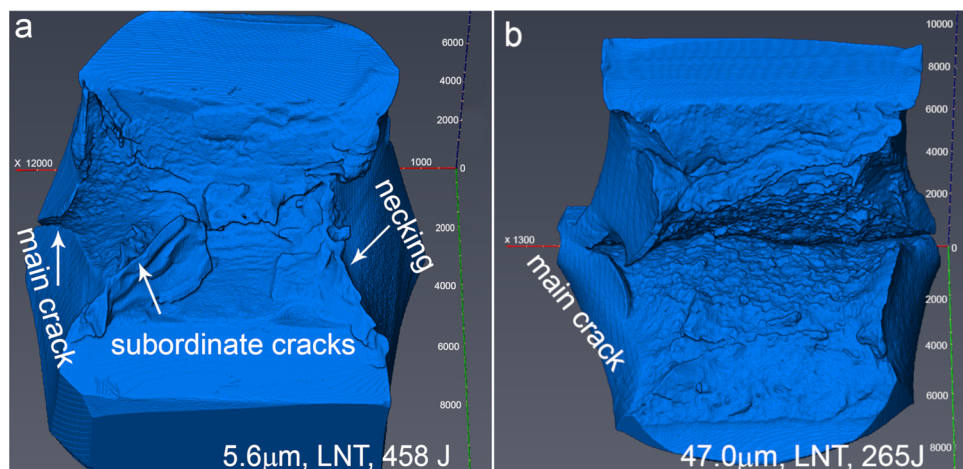


Fig. 4 3D fracture surface morphology using micro-computed tomography of fine- and coarse-grained samples after Charpy impact testing at LNT. **a** A big neck is formed at the fracture surface in fine-grained sample after impact testing at LNT, with a main crack seen along the direction of the Charpy notch and subordinate cracks lying perpendicular to the direction of the Charpy notch (see Supplementary Fig. 4). **b** Single deep crack along the direction of the Charpy notch in a coarse-grained sample after impact testing at LNT where no necking is seen and the fracture surface is flat.

Table 3 Quantification of microstructural damage after Charpy impact testing at LNT.

Sample	Deformation at neck	Deformation at back side	Crack depth (mm)	Deformation near the notch opening
5.6 μm, LNT	-33.6%	25.2%	1.62	-5.3%
47.0 μm, LNT	-31.1%	22.4%	5.54	-0.4%

Values of plastic deformation defined by change in length along lines parallel to the notch line, with positive values indicating tension—see “Methods” section for a more detailed description of these definitions.

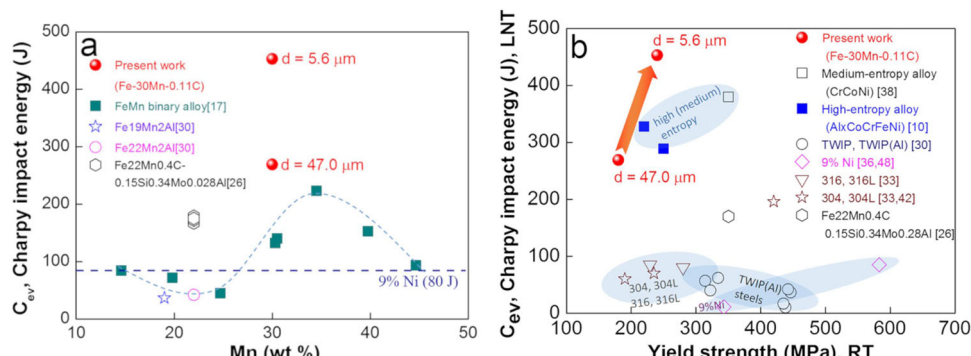


Fig. 5 Comparison with various cryogenic metals. **a** Comparison of Charpy impact toughness with different manganese steels at LNT; the horizontal blue line shows the GB 24510-2009 standard of 9% Ni for plate of thickness ≤ 30 mm. **b** Charpy impact energy at LNT as a function of RT yield strength. The grain sizes for the samples referenced in **b** are all in the range of 7.5–50 μm.

these steels at LNT remains worse than that at RT, i.e., the second criterion mentioned above is not fulfilled. Accordingly, the impact toughness for these steels decreases with decreasing temperature, in a manner similar to that for standard steels^{1,26}. It should be noted, however, that for the present coarse-grained sample, the impact toughness also decreases with decreasing temperature, despite the fact that a transition from planar slip to twinning, and an increase in both tensile strength and ductility, are observed with decreasing temperature. This result clearly indicates that the two criteria mentioned above are necessary, but not sufficient, to ensure an inverted temperature-toughness dependence. For high-Mn carbon steels, the preventing the formation of ϵ martensite is also important.

In austenitic steels, the stacking fault energy (SFE) energy is typically used to explain the deformation tendency: low SFE (<20 mJ/m²) favors phase transformations (from γ to ϵ or α' phase), medium SFE (20–45 mJ/m²) favors deformation twinning, and high SFE (>45 mJ/m²) favors slip. For the present case, both the C content and grain size²⁵, as well as the testing temperature, affect the SFE. The SFE values for the two samples at the two test temperatures have been calculated theoretically based on a thermodynamic model, and are listed in Table 4 (details regarding the calculation procedure can be found in the Supplementary Note 1). Although the precise calculated SFE values depend on grain boundary energy values, the overall trend of the SFE as a function of grain size and test temperature will not change if

Table 4 Calculated stacking fault energy for the fine- and coarse-grained samples at both RT and LNT.

Mean grain size (μm)	RT	LNT
5.6 \pm 1.7	28.5 mJ m^{-2}	23.8 mJ m^{-2}
47.0 \pm 4.0	21.9 mJ m^{-2}	17.2 mJ m^{-2}

different grain boundary energy values are used. As such a transition from ϵ martensite to mechanical twinning, and then to slip, as evidenced experimentally in Figs. 2 and 3, is clearly explained by the trend in SFE values.

Following this SFE trend, the comparatively low impact toughness for conventional 304(L) at LNT can be understood. The SFE for conventional 304(L) with grain size around 50 μm is typically lower than 18–20 mJ m^{-2} ⁴¹, facilitating α' - or ϵ -martensite transformation⁴². A combination of some additional amount of C and grain refinement, as used for the present high-Mn steel, may also be a solution for the 304(L) to reverse the temperature-toughness dependence. However, there is also an upper limit of the SFE, typically \sim 45 mJ m^{-2} , above which mechanical twinning is severely retarded and ductility decreases with decreasing temperature. Heterogeneous plastic deformation-induced sole by dislocation slip can also result in large stress concentrations at grain boundaries and hence lead to intergranular fracture, as observed in Fe36Mn¹⁵. This is also likely to be the reason for comparatively low impact toughness for conventional 316(L)³³ with SFE typically higher than 45 mJ m^{-2} . In this case, grain refinement can reduce slip-based deformation heterogeneity within grains, but is unlikely to reverse the temperature-toughness dependence, as mechanical twinning will not operate. The SFE of a CoCrNi MEA with a grain size of 16 μm , measured based on TEM micrographs, was estimated as $22 \pm 4 \text{ mJ m}^{-2}$, which is lower than that for a CrMnFeCoNi HEA with a similar grain size, $30 \pm 5 \text{ mJ m}^{-2}$ ⁴³. For the CoCrNi MEA included in Fig. 5b with a grain size of \sim 9.5 μm (taking twin boundaries into account)³⁸, the SFE will be slightly higher than $22 \pm 4 \text{ mJ m}^{-2}$, and may be similar to that of the fine-grained Fe-30Mn-0.11C steel. Similarly, the SFE for the CoCrFeNi HEA¹⁰ is expected to be in between 22 and $30 \pm 5 \text{ mJ m}^{-2}$, close to that of the fine-grained Fe-30Mn-0.11C steel. Similar deformation mechanisms between these three alloys can therefore be rationalized. As such grain refinement may further improve the impact energy of the CoCrNi and CoCrFeNi M/HEAs. In contrast, in the $\text{Al}_x\text{CoCrFeNi}$ HEAs¹⁰ the small additions of Al (0.1–0.3%) will increase the SFE, which in combination with some further SFE increase by grain refinement to \sim 7.5 μm , can be expected to result in a decrease in the extent of mechanical twinning, thus leading to the reduced impact energy of these alloys¹⁰ compared to the CoCrFeNi alloy.

On top of the SFE, both the mechanical twinning and ϵ -martensite transformation are orientation dependent⁴⁴. Although this does not contribute much to the differences observed for the present two samples as they possess similar texture, it is still useful to keep in mind the possibility in future work for tailoring the texture of the samples to achieve grains with <111> parallel to the tensile axis, thereby facilitating mechanical twinning⁴⁴.

The present result also shows a significant influence of strain rate on the microstructural evolution (comparing Figs. 2 with 3). Strain rate is usually coupled with temperature effects in materials science by an Arrhenius type equation, which is characteristic of a thermally activated process. For twinning and ϵ -martensite transformation, which essentially involves stacking fault processes, the effects of increasing strain rate are expected to be equivalent to those of lowering temperatures⁴⁵. Tensile tests

conducted at strain rates more similar to those relevant for impact testing may be more accurate as a predictor of impact behavior.

In the investigated alloy, there is only limited direct contribution from mechanical twinning to the plastic strain⁴⁶. Twin boundaries certainly subdivide the grains into twinned and untwinned regions, which can effectively reduce the dislocation mean free path and acts as strong planer obstacles for dislocation motion (i.e., a dynamic Hall-Petch effect)⁴⁶. At the same time, however, the slip systems in operation in the twins and matrix are different, and the twin boundaries react in various ways with impinged dislocations (e.g., ref. ⁴⁷), which can reduce stress concentrations and postpone the formation of local necking or crack nucleation.

It can also be noted that the coherent twin boundaries are much stronger interfaces than those between the ductile γ and brittle ϵ phases, where the latter are typically associated with stress concentrations. Higher interfacial strength can retard both the crack nucleation and propagation. Similarly, grains that have undergone mechanical twinning and that contain nanotwin bundles are very strong barriers for blocking cracks propagating perpendicular to the twin boundary, and thereby promoting crack branching⁴⁸.

High-Mn steels have good potential for cryogenic applications, taking account of various properties including corrosion resistance, fatigue resistance, and the strength of welded joints¹. In this regard, a limitation of the present Fe-30Mn-0.11C steel is that this alloy has a comparatively lower yield stress than some alternative cryogenic steels and the competing HEAs/MEAs (see Fig. 5b). A key factor here is the relatively low Hall-Petch slope of this type of austenitic Fe–Mn–C steel³², such that the strength increase by grain refinement is therefore relatively low compared to that achievable in ferritic steels. Although not yet explored, it can be expected that the strength may be improved by further adjustment of the alloy composition, specifically increasing the C content at a constant or reduced Mn content, or by adding a small amount of Al²⁹, to enhance solute hardening in the alloy while keeping the SFE unchanged or only slightly increased. In this regard, it is known that mechanical twinning is still prevalent in 30% Mn steels with carbon content up to 0.6%^{21,40}. Also, even if the impact toughness is influenced by a strength increase, it is expected that as long as the formation of α' and ϵ martensitic remains suppressed by tailoring of the grain size, the inverse temperature dependence of toughness can be preserved. In a recent study⁴⁹, it has been demonstrated that the yield strength at RT in a Fe-34Mn-0.04C steel can be varied by microstructural design over a wide range of 200–780 MPa, with tensile elongation comparable to 9% Ni steel at each corresponding yield strength level. Combined with the present work, this indicates a possible route to achieve high yield strength Fe–Mn–C steels with comparable or even better impact toughness than 9Ni steels or CoCrFeNi HEAs/CoCrNi MEAs, but at a much lower cost.

In this regard it can be noted that based on data from the London Metal Exchange, the price of Ni over the last few years has varied from 5 to 10 times higher than that for Mn, with an even greater differential to the price of Co (11–50 times higher price than Mn) (<https://www.lme.com/>). The high cost of Co has been driven up in recent years in particular as a result of the increased demand for batteries to provide automotive power in electric vehicles⁵⁰. As such, even when used in relatively large amounts as in the present alloy, Mn can be used to replace expensive additions of Ni and Co, allowing the production of a high performance cryogenic alloy at a significantly lower cost.

Conclusions. In summary, the present study demonstrates the possibility to obtain high-Mn, low-carbon steels with superior

cryogenic toughness. By a combination of these austenite stabilizing elements, together with an appropriately fine-grain size, an inverse temperature dependence of toughness has been realized resulting in a cryogenic toughness of >450 J achieved in the fine-grained Fe-30Mn-0.11C steel. In contrast to high entropy alloys with high cryogenic toughness, the low price of Mn and the suitability for industrial mass production using conventional processing routes combine to make this fine-grained Fe-Mn-C alloy with superior toughness a very cost-effective steel for a wide range of cryogenic applications.

Methods

Sample preparation. The investigated steel was melted using vacuum induction with a main chemical composition of Fe-30Mn-0.11C (wt. pct). The ingot was heated to 1000 °C and held for 1 h, and then forged at 800–1000 °C to produce 20 mm thick plate. The hot forged plate was heated at 1000 °C for 1 h to obtain a coarse grain size of 47.0 µm. The hot forged plate was then cold rolled to a thickness reduction of 50% and followed by annealing at 700 °C for 2 h to obtain fully recrystallized grains with a fine-grain size of 5.6 µm.

Microstructural characterization. Microstructural analyses were carried out using a field emission SEM equipped with a backscattered electron detector and an EBSD system operated at an accelerating voltage of 20 kV both for microstructure characterization and fracture morphology investigation. The microstructure was also characterized by transmission electron microscopy using a JEM-2100 electron microscope operated at 200 kV.

Mechanical property tests. Conventional uniaxial tensile tests with the tensile axis aligned along the rolling direction of the initial plate were carried using a MTS tensile testing machine, equipped with a chamber to carry out deformation at low temperatures. Tensile specimens with a gauge length of 10 mm, width of 2 mm, and thickness of 2 mm were prepared from the annealed treated plates. Tensile tests were carried out at an initial strain rate of 10^{-3} s^{-1} at RT and LNT. For each condition three specimens were tested, and the average value was used. Charpy impact tests were carried out using an ASTM standard E_23 tester (samples with dimensions of $10 \times 10 \times 55 \text{ mm}^3$), and with a 2 mm deep V-notch at the center at RT and LNT by a MTS impact tester of 600 J capacity. To increase the accuracy of this procedure, the hammer was released only if the entire process occurred within 5 s. Three specimens were tested, and the average value was used. Samples tested at LNT were precooled directly in liquid nitrogen; the time between taking a sample out of the cooling bath and actual impact for all recorded data was less than 5 s. Deformation of the impact-tested samples was quantified by measuring the change in length parallel to the notch line (i) on the notch surface near the notch opening, (ii) near the notch tip, and (iii) on the back surface of the sample in a location behind the notch tip.

3D fracture surface morphology. To reveal the 3D morphology of the fractured surface, the samples after Charpy impact tests were characterized by X-ray CT using a Zeiss Xradia 520 Versa micro-CT system. For the CT scans, a polychromatic conical beam with X-ray energies up to 150 keV, an exposure time of 10 s, and 3001 image projections over a rotation of 360° were used. The voxel size of the scanned 3D volume was 13.3 µm. Visualization and analysis of the 3D fractured samples were conducted using Avizo®.

Data availability

The experimental data included in this study are available upon reasonable request from the corresponding authors.

Received: 22 August 2020; Accepted: 19 March 2021;

Published online: 21 April 2021

References

- Choi, J. K., Lee, S.-G., Park, Y.-H., Han, I.-W. & Morris, J. W. Jr. High manganese austenitic steel for cryogenic applications. In *Proc. 22nd International Offshore and Polar Engineering Conference* 29–35 (Rhodes, Greece, 2012).
- Leighly, H. P., Bramfitt, B. L. & Lawrence, S. J. RMS Titanic: a metallurgical problem. *Pract. Fail. Anal.* **1**, 10–13 (2001).
- Kimura, Y., Inoue, T., Yin, F. X. & Tsuzaki, K. Inverse temperature dependence of toughness in an ultrafine grain-structure steel. *Science* **320**, 1057–1060 (2008).
- Morris, J. W. Jr., Guo, Z., Krenn, C. R. & Kim, Y.-H. The limits of strength and toughness in steel. *ISIJ Int.* **41**, 599–611 (2001).
- Stolyarov, V. V., Valiev, R. Z. & Zhu, Y. T. Enhanced low-temperature impact toughness of nanostructured Ti. *Appl. Phys. Lett.* **88**, 041905 (2006).
- Das, P., Jayaganthan, R. & Singh, I. V. Tensile and impact-toughness behaviour of cryorolled Al 7075 alloy. *Mater. Des.* **32**, 1298–1305 (2011).
- Kern, A., Schriever, U. & Stumpfe, J. Development of 9% nickel steel for LNG applications. *Steel Res. Int.* **78**, 189–194 (2007).
- Wu, S. J., Sun, G. J., Ma, Q. S., Shen, Q. Y. & Xu, L. Influence of QLT treatment on microstructure and mechanical properties of a high nickel steel. *J. Mater. Process. Tech.* **213**, 120–128 (2013).
- Li, D. Y. & Zhang, Y. The ultrahigh charpy impact toughness of forged AlxCrFeNi high entropy alloys at room and cryogenic temperatures. *Intermetallics* **70**, 24–28 (2016).
- Li, R. X. & Zhang, Y. *Entropic Alloys for Cryogenic Applications, Stainless Steels and Alloys* (ed. Duriagina, Z) (IntechOpen, 2019). <https://doi.org/10.5772/intechopen.82351>.
- Morris, J. W. Jr. Making steel strong and cheap. *Nat. Mater.* **16**, 787–789 (2017).
- Li, Z., Pradeep, K. G., Deng, Y., Raabe, D. & Tasan, C. C. Metastable high-entropy dual-phase alloys overcome the strength-ductility trade-off. *Nature* **534**, 227–30 (2016).
- Grässel, O., Krüger, L., Frommeyer, G. & Meyer, L. W. High strength Fe±Mn ±(Al, Si) TRIP/TWIP steels development – properties – application. *Int. J. Plast.* **16**, 1391–1409 (2000).
- Seol, J. B., Jung, J. E., Jiang, Y. W. & Park, C. G. Influence of carbon content on the microstructure martensitic transformation and mechanical properties in austenite/e-martensite dual-phase Fe-Mn-C steels. *Acta Mater.* **61**, 558–578 (2013).
- Tomota, Y., Strum, M. & Morris, J. W. Jr. Microstructural dependence of Fe-high Mn tensile behavior. *Metall. Mater. Trans.* **17A**, 537–547 (1986).
- Tomota, Y., Strum, M. & Morris, J. W. The relationship between toughness and microstructure in Fe-High Mn binary alloys. *Metall. Mater. Trans.* **18A**, 1073–1081 (1987).
- Koyama, M., Sawaguchi, T. & Tsuzaki, K. Premature fracture mechanism in an Fe-Mn-C austenitic steel. *Metall. Mater. Trans.* **43A**, 4063–4074 (2012).
- De Moor, E., Matlock, D. K., Speer, J. G. & Merwin, M. J. Austenite stabilization through manganese enrichment. *Scr. Mater.* **64**, 185–188 (2011).
- Koyama, M., Sawaguchi, T., Lee, T., Lee, C. S. & Tsuzaki, K. Work hardening associated with ε-martensitic transformation, deformation twinning and dynamic strain aging in Fe-17Mn-0.6C and Fe-17Mn-0.8C TWIP steels. *Mat. Sci. Eng. A* **528**, 7310–7316 (2011).
- Seol, J.-B., Jung, J. E., Jang, Y. W. & Park, C. G. Influence of carbon content on the microstructure, martensitic transformation and mechanical properties in austenite/e-martensite dual-phase Fe-Mn-C steels. *Acta Mater.* **61**, 558–578 (2013).
- Ghasri-Khouzani, M. & McDermid, J. R. Microstructural evolution and mechanical behaviour of Fe-30Mn-C steels with various carbon contents. *Mater. Sci. Technol.* **33**, 1159–1170 (2017).
- Tomota, Y., Strum, M. & Morris, J. W. Tensile deformation behavior of mechanically stabilized Fe-Mn austenite. *Metall. Mater. Trans.* **19A**, 1564–1568 (1988).
- Lee, Y.-K. & Choi, C.-S. Driving force for $\gamma \rightarrow \epsilon$ martensitic transformation and stacking fault energy of γ in Fe-Mn binary system. *Metall. Mater. Trans.* **31A**, 355–360 (2000).
- Takaki, S., Nakatsu, H. & Tokunaga, Y. Effects of austenite grain size on ϵ martensitic transformation in Fe-15mass% Mn alloy. *Mater. Trans. JIM* **34**, 489–495 (1993).
- Jun, J.-H. & Choi, C.-S. Variation of stacking fault energy with austenite grain size and its effect on the Ms temperature of $\gamma \rightarrow \epsilon$ martensitic transformation in Fe-Mn alloy. *Mater. Sci. Eng. A* **257**, 353–356 (1998).
- Wang, X. J. et al. Grain size-dependent mechanical properties of a high-manganese austenitic steel. *Acta Metall. Sin.* **32**, 746–754 (2019).
- Dini, G., Najafizadeh, A., Ueji, R. & Monir-Vaghefi, S. M. Tensile deformation behavior of high-manganese austenitic steel: the role of grain size. *Mater. Des.* **31**, 3395–3402 (2010).
- Liang, X. et al. Microstructural evolution and strain hardening of Fe-24Mn and Fe-30Mn alloys during tensile deformation. *Acta Mater.* **57**, 3978–3988 (2009).
- Sato, K., Ichinose, M., Hirotsu, Y. & Inoue, Y. Effects of deformation induced phase transformation and twinning on the mechanical properties of austenitic Fe-Mn-Al alloys. *ISIJ Int.* **29**, 868–877 (1989).
- Sohn, S. S. et al. Effects of Mn and Al contents on cryogenic-temperature tensile and Charpy impact properties in four austenitic high-Mn steels. *Acta Mater.* **100**, 39–52 (2015).
- Koyama, M., Lee, T., Lee, C. S. & Tsuzaki, K. Grain refinement effect on cryogenic tensile ductility in a Fe-Mn-C twinning-induced plasticity steel. *Mater. Des.* **49**, 234–241 (2013).

32. Wang, Y. H. et al. Hall-Petch strengthening in Fe-34.5Mn-0.04C steel cold-rolled, partially recrystallized and fully recrystallized. *Scr. Mater.* **155**, 41–45 (2018).
33. Nam, Y.-H., Park, J.-S., Baek, U.-B., Suh, J.-Y. & Nahm, S.-H. Low-temperature tensile and impact properties of hydrogen-charged high-manganese steel. *Int. J. Hydrogen Energy* **44**, 7000–7013 (2019).
34. Byun, T. S., Hashimoto, N. & Farrell, K. Temperature dependence of strain hardening and plastic instability behaviors in austenitic stainless steels. *Acta Mater.* **52**, 3889–3899 (2004).
35. Tomota, Y., Xia, Y. & Inoue, K. Mechanism of low temperature brittle fracture in high nitrogen bearing austenitic steels. *Acta Mater.* **46**, 1577–1587 (1998).
36. Kwon, K. H. et al. Origin of intergranular fracture in martensitic 8Mn steel at cryogenic temperatures. *Scr. Mater.* **69**, 420–423 (2013).
37. Xia, S. Q., Gao, M. C. & Zhang, Y. Abnormal temperature dependence of impact toughness in Al CoCrFeNi system high entropy alloys. *Mater. Chem. Phys.* **210**, 213–221 (2018).
38. Yang, M. X. et al. High impact toughness of CrCoNi medium-entropy alloy at liquid-helium temperature. *Scr. Mater.* **172**, 66–71 (2019).
39. Jo, Y. H. et al. Cryogenic strength improvement by utilizing room-temperature deformation twinning in a partially recrystallized VCrMnFeCoNi high-entropy alloy. *Nat. Commun.* **8**, 15719 (2017).
40. Wang, X., Zurob, H. S., Embury, J. D., Ren, X. & Yakubtsov, I. Microstructural features controlling the deformation and recrystallization behavior Fe-30%Mn and Fe-30Mn-0.5C. *Mater. Sci. Eng. A* **527**, 3785–3791 (2010).
41. Talonen, J. & Hanninen, H. Formation of shear bands and strain-induced martensite during plastic deformation of metastable austenitic stainless steels. *Acta Mater.* **55**, 6108–6118 (2007).
42. Zheng, C. S. & Yu, W. W. Effect of low-temperature on mechanical behavior for an AISI 304 austenitic stainless steel. *Mater. Sci. Eng. A* **710**, 359–365 (2018).
43. Laplanche, G. et al. Reasons for the superior mechanical properties of medium-entropy CrCoNi compared to high-entropy CrMnFeCoNi. *Acta Mater.* **128**, 292–303 (2017).
44. Gutierrez-Urrutia, I., Zaeferer, S. & Raabe, D. The effect of grain size and grain orientation on deformation twining in a Fe-22wt.% Mn-0.6wt.% C TWIP steel. *Mater. Sci. Eng. A* **527**, 3552–3560 (2010).
45. Christian, J. W. & Mahajan, S. Deformation twinning. *Prog. Mater. Sci.* **39**, 1–157 (1995).
46. Qin, B. & Bhadeshia, H. K. D. H. Plastic strain due to twinning in austenitic TWIP steels. *Mater. Sci. Technol.* **24**, 969–973 (2008).
47. Lu, K., Lu, L. & Suresh, S. Strengthening materials by engineering coherent internal boundaries at the nanoscale. *Science* **324**, 349–352 (2009).
48. Xiong, L., You, Z. S., Qu, S. D. & Lu, L. Fracture behavior of heterogeneous nanostructured 316L austenitic stainless steel with nanotwin bundles. *Acta Mater.* **150**, 130–138 (2018).
49. Wang, Y. H. *Microstructural Control for Enhancing the Mechanical Properties of High Mn Austenitic Steel at Ambient and Cryogenic Temperatures*. Ph.D. thesis, Yanshan Univ. (2018).
50. Dunn, B., Kamath, H. & Tarascon, J.-M. Electrical energy storage for the grid: a battery of choices. *Science* **334**, 928–935 (2011).

Acknowledgements

The authors gratefully acknowledge the support from the National Nature Science Foundation of China (Grant Nos 51871194 and 51971117) and the National Natural Foundation of Hebei Province, China (Grant no. E2018203312). X.H. thanks the support of National Key Research and Development Program of China (2016YFB0700403, 2016YFB0700401). N.H. thanks the support of the 111 Project (B16007) by the Ministry of Education and the State Administration of Foreign Experts Affairs of China. Y.Z. acknowledges the support from the European Research Council (ERC) under the European Union's Horizon 2020 research and innovation programme (grant agreement no. 788567, M4D).

Author contributions

Y.W., X.H., and A.G. conceived the study. Y.W., Y.P., and T.W. performed mechanical tests and TEM characterization. J.K. performed EBSD characterization. Y.Z. performed 3D fracture surface morphology measurements. Y.W., T.W., and Y.Z. analyzed the data. and Y.W., A.G., Y.Z., N.H., and X.H. wrote the manuscript. All authors discussed the results and commented on the manuscript.

Competing interests

The authors declare no competing interests.

Additional information

Supplementary information The online version contains supplementary material available at <https://doi.org/10.1038/s43246-021-00149-8>.

Correspondence and requests for materials should be addressed to A.G. or X.H.

Peer review information Primary handling editor: John Plummer.

Reprints and permission information is available at <http://www.nature.com/reprints>

Publisher's note Springer Nature remains neutral with regard to jurisdictional claims in published maps and institutional affiliations.



Open Access This article is licensed under a Creative Commons Attribution 4.0 International License, which permits use, sharing, adaptation, distribution and reproduction in any medium or format, as long as you give appropriate credit to the original author(s) and the source, provide a link to the Creative Commons license, and indicate if changes were made. The images or other third party material in this article are included in the article's Creative Commons license, unless indicated otherwise in a credit line to the material. If material is not included in the article's Creative Commons license and your intended use is not permitted by statutory regulation or exceeds the permitted use, you will need to obtain permission directly from the copyright holder. To view a copy of this license, visit <http://creativecommons.org/licenses/by/4.0/>.

© The Author(s) 2021